Flexural buckling behaviour of concrete-filled double skin aluminium alloy columns

Shafayat Bin Ali [a,b,*], George S. Kamaris [a], Michaela Gkantou [a]

[a] *School of Civil Engineering and Built Environment, Liverpool John Moores University, Liverpool, L3 3AF, United Kingdom*
[b] *Institute of Earthquake Engineering Research, Chittagong University of Engineering & Technology, Chattogram 4349, Bangladesh*

A R T I C L E I N F O

A B S T R A C T

Concrete-filled double skin steel tubular columns consisting of two hollow steel tubes and concrete infill between their interspace, have become popular in modern construction owing to their high ultimate load, less self-weight and good ductility. The weight of these columns can be reduced further by using lightweight aluminium alloy hollow tubes instead of steel ones. This paper experimentally and numerically studied the flexural buckling behaviour of the concrete-filled double skin aluminium tubular (CFDSAT) columns subjected to axial compression. A total of 8 CFDSAT columns were tested using a pin-ended set-up. The test results are presented in terms of failure modes, ultimate load and load versus mid-height lateral displacement curves. Non-linear finite element (FE) models of the specimens were developed and their accuracy was evaluated by comparing the FE and test results. A numerical parametric investigation was conducted to study the influence of the hollow ratio, the member slenderness, the cross-sectional slenderness of the hollow tubes and the concrete strength on the structural behaviour of CFDSAT columns. The parametric study results revealed that the cross-sectional dimensions of outer section, the member slenderness and the concrete compressive strength have a significant effect on the flexural buckling response of the columns, while the influence of the cross-sectional dimensions of inner section is less prominent. In the absence of design standards for CFDSAT members, a design methodology is proposed with a design buckling curve to predict the ultimate load of CFDSAT columns based on the Eurocode 4 framework. Moreover, a revised concrete correction factor is suggested to determine the effective flexural rigidity of CFDSAT columns according to Eurocode 4.

1. Introduction

Concrete-filled double skin steel tubular (CFDSST) column is fabricated using two hollow steel tubes and the space between them is filled with concrete. CFDSST columns have several benefits compared to the conventional concrete-filled steel tubular (CFST) ones, such as, less self-weight because of the absence of inner concrete [1], good global and local stability owing to the beneficial composite action [2] and better fire resistance due to thermal protection provided by the outer hollow section to the inner hollow section and concrete [3]. Aluminium alloys are versatile metals with a combination of superior properties, including, high strength-to-weight ratio, excellent corrosion resistance, good formability and attractive appearance [4–6]. Hence, the use of aluminium alloy tubes in the concrete-filled double skin sections can further reduce their weight significantly and enhance their resilience. On the other hand, the structural stability of aluminium alloy hollow

sections can improve remarkably by incorporating the concrete infill [7–9]. Therefore, by combining the effectiveness of double skin technique and the profound features of aluminium alloys, a concrete-filled double skin aluminium alloy tubular (CFDSAT) column can be an efficient structural member for structures located in aggressive environments, such as offshore wind turbines, offshore oil platforms, seaside piers, containment building of nuclear power plants, tall buildings and bridges in earthquake-prone regions.

A number of research studies are available on the structural behaviour of CFDSST columns. Experimental investigations were performed to study the compressive behaviour of CFDSST short columns comprised carbon steel square [10], rectangular [11] and circular [12–14] outer and inner profiles. In these studies, the failure pattern of CFDSST columns was investigated and design guidelines were suggested to calculate the ultimate capacity of the columns. Elchalakani et al. [15] and Han et al. [16] tested CFDSST stub columns produced by cold-formed steel circular-square and square-circular outer and inner tubes and

---

Nomenclature

A_c	area of concrete
A_o	area of outer tube
A_i	area of inner tube
B_o	width of outer tube
B_i	width of inner tube
D_o	depth of outer tube
D_i	depth/diameter of inner tube
E	modulus of Elasticity
EI_e	effective flexural rigidity of column
e_0	initial loading eccentricity
f	tensile stress
f_c	concrete cylinder compressive strength
f_{cu}	concrete cube compressive strength
f_u	ultimate tensile stress
$f_{0.1}$	0.1 % proof stress
$f_{0.2}$	0.2 % proof stress
I	moment of inertia of cross-section
k_e	concrete correction factor
L	length of column
L_e	effective length of column
N_{cr}	critical buckling load or Euler's critical load of column
N_{pl}	plastic resistance of column under axial compression
N_u	ultimate load of column obtained from test and FE analysis
$N_{u,FE}$	ultimate load of column obtained from FE analysis
$N_{u,prop}$	design ultimate load of column
$N_{u,Test}$	ultimate load of tested column
n	strain hardening exponent
t_o	thickness of outer tube
t_i	thickness of inner tube
α	hollow ratio
α_1	imperfection factor
δ	lateral deflection at the mid-height of column
ε	strain under tension
ε_f	strain at fracture
ε_{max}	maximum strain
ε_{min}	minimum strain
ε_u	strain at ultimate tensile stress
$\bar{\lambda}$	member slenderness
$\bar{\lambda}_0$	limit of horizontal plateau
ϕ	a parameter
χ	reduction factor for determining flexural buckling capacity of column
ω_g	initial global imperfection amplitude

---

recommended design formulae for these columns. A series of compressive tests were conducted on CFDSST stub columns made with square-rectangular [17], circular [18], square-circular [19] and round-up rectangular-elliptical [20] carbon steel inner and stainless steel outer sections. These research studies suggested design rules for the aforementioned compression members. Wang et al. [21] numerically investigated the compressive response of square CFDSST cross-sections constructed with stainless outer hollow sections and proposed modifications of the current design standards to predict their design strength. Tziavos et al. [22] conducted a numerical study to examine the compressive response of grout-filled double-skin tubular steel short columns and suggested design equations for these columns. Zhao et al. [23], Han et al. [24] and Zheng et al. [25] investigated the behaviour of CFDSST short columns subjected to large axial deformation, long-term sustained load and cyclic load. Research on the compressive behaviour of CFDSST slender columns was carried out by Hassanein and Kharoob [26], Sulthana and Jayachandran [27], Zhao et al. [28] and Ahmed et al. [29] considering different cross-sectional shapes and steel materials. They suggested a design equation to determine the ultimate capacity of these columns.

Few studies exist on the compressive response of CFDSAT stub columns. Zhou and Young [30,31] experimentally and numerically studied the influence of geometry and concrete strength on the structural response of 6061-T6 alloy CFDSAT stub columns made with circular and circular-square outer and inner profiles. They recommended design guidelines to determine the compressive capacity of these cross-sections. Patel et al. [32] conducted a numerical study on the structural behaviour of CFDSAT short columns using a fiber element model and proposed a formula to evaluate the lateral confining pressure developed on the concrete infill. However, no research study is available on the buckling response of CFDSAT columns so far. Hence, this paper reports for the first time an experimental and numerical study on the flexural buckling response of CFDSAT members under axial compression. The hollow tubes used in this study were manufactured by 6082-T6 aluminium alloy which is a popular alloy owing to its high strength, excellent resistance to corrosion and good weldability [7,33]. In this paper, the test programme and the obtained test findings are presented in Sections 2 and 3, respectively. In Section 4, non-linear finite element (FE) models of the specimens are developed and a numerical parametric study is conducted. In Section 5, a design methodology is proposed on the basis of Eurocode 4 [34]. Finally, in Section 6, conclusions are provided.

2. Test programme

2.1. CFDSAT specimens

A total of 8 CFDSAT columns were tested under axial compression, in which 6 specimens comprised square outer and inner tubes and 2 specimens were made with square outer and circular inner tubes. The hollow tubes were manufactured by 6082-T6 grade aluminium alloy, except two inner tubes, i.e., S19.2 × 1.6 and C19.2 × 3.2 which were produced by 6063-T6 aluminium alloy. Fig. 1 illustrates the cross-sectional geometry of typical specimens and Table 1 presents the measured geometric dimensions of all specimens, including depth/diameter (D), width (B) and thickness (t), where the subscripts 'o' and 'i' represent the outer and inner hollow sections, respectively. Moreover, the cross-section class of the outer and the inner tubes based on Eurocode 9 [35] and column slenderness ($\bar{\lambda}$) determined according to Eurocode 4 [34] (see Equation (8) in Section 5.1) are also provided in Table 1. In this study, 8 hollow sections were taken in total, where three large sections with measured depth/diameter to thickness ratio (D_o/t_o) varying from 16.45 to 20.81 were utilised as the outer profiles and five small sections with measured depth/diameter to thickness ratio (D_i/t_i) ranging from 6.09 to 16.74 were utilised as the inner profiles. All specimens were 1000 mm long. The nominal effective length (L_e) of the specimens, including pin-ended supports, was 1064 mm. The specimens were labelled considering the geometric dimensions of the outer and the inner hollow sections. For example, the label 'S63.4 × 3.2-C19.2 × 3.2' indicates a CFDSAT specimen consisting of 'S63.4 × 3.2' outer section and 'C19.2 × 3.2' inner section. In the notation 'S63.4 × 3.2', the letter 'S' signifies that the hollow section is square with nominal depth and width of 63.4 mm and thickness of 3.2 mm. In the notation 'C19.2 × 3.2', the letter 'C' represents a circular hollow section which has a nominal diameter of 19.2 mm and thickness of 3.2 mm.

Before concrete casting, the inner tubes of all specimens were precisely located at the centroid of the outer hollow section using top and bottom wooden plates. The wooden plates were prepared by attaching two parts, i.e., an outer part and an inner part. The dimensions of the
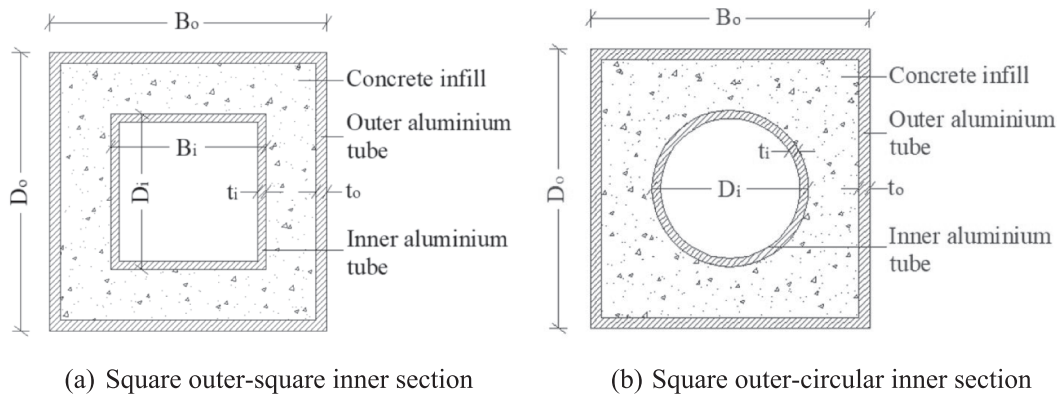
(a) Square outer-square inner section   (b) Square outer-circular inner section

Fig. 1. Cross-sectional geometry of typical CFDSAT specimens.

Table 1
Measured cross-sectional dimensions, cross-section class of hollow tubes, member slenderness and initial global geometric imperfection of CFDSAT specimens.

Specimen	D_o (mm)	B_o (mm)	t_o (mm)	D_o/t_o	Class of outer section	D_i (mm)	B_i (mm)	t_i (mm)	D_i/t_i	Class of inner section	$\bar{\lambda}$	ω_g (mm)
S50.8 × 3.2-S19.2 × 1.6	50.83	50.83	3.09	16.45	2	19.05	19.05	1.53	12.45	1	1.08	0.27
S63.4 × 3.2-S19.2 × 1.6	63.48	63.48	3.05	20.81	2	19.06	19.06	1.53	12.46	1	0.73	0.15
S63.4 × 3.2-S25.4 × 3.2	63.48	63.48	3.06	20.75	2	25.38	25.38	3.28	7.74	1	0.80	0.39
S76.2 × 4.8-S19.2 × 1.6	76.09	76.09	4.61	16.51	3	19.05	19.05	1.57	12.13	1	0.75	0.11
S76.2 × 4.8-S25.4 × 1.6	76.09	76.09	4.58	16.61	3	25.27	25.27	1.51	16.74	2	0.75	0.04
S76.2 × 4.8-S25.4 × 3.2	76.09	76.09	4.61	16.51	3	25.42	25.42	3.30	7.70	1	0.78	0.07
S63.4 × 3.2-C19.2 × 3.2	63.54	63.45	3.10	20.50	2	18.88	–	3.10	6.09	1	0.77	0.12
S63.4 × 3.2-C25.4 × 3.2	63.48	63.45	3.08	20.61	2	25.41	–	3.37	7.54	1	0.76	0.30

outer part were similar to the dimensions of the outer hollow section, whereas the dimensions of the inner part were the same as the dimensions of the interspace between two tubes of the respective specimen (Fig. 2(a)). The top end of the inner tubes was closed with plastic tape to avoid concrete falling inside them during casting. To avoid any concrete leakage the bottom wooden plates were sealed properly. The casting was conducted by filling concrete in layers. The concrete was compacted using a vibrating table. After the cast, the columns were covered using a plastic sheet to avoid moisture loss from the concrete. The columns were cured for 28 days and then the wooden plates were separated from both ends. Fig. 2 shows photos of the wooden plates and the typical cross-sections of the specimens.

The initial global geometric imperfection (ω_g) has a strong effect on the buckling behaviour and load-bearing capacity of slender columns [29]. Therefore, prior to the test the values of ω_g of all specimens were measured using a linear height gauge and considered in the numerical investigation reported in Section 4. The value of ω_g corresponding to the buckling axis was defined by determining the deviation at the mid-length of a face parallel to the buckling axis from the reference line connecting both ends of a specimen [7]. The recorded values of ω_g are listed in Table 1.

2.2. Material properties

2.2.1. Aluminium alloy hollow section
Tensile coupon tests were performed to determine the material properties of aluminium alloy hollow tubes. Two coupons were cut longitudinally from the square (dogbone flat coupons) and the circular (curved coupons) tubes by following the guidance given in BS EN ISO

6892–1 [36]. A 50 kN hydraulic tensile machine was used for the tests. During the tests, flat grip faces were used for the flat coupons (Fig. 3(a)) and grip faces with a pitch serration were applied for the curved coupons for ensuring better contact between the specimen and the grip faces (Fig. 3(b)). A displacement-control load with a rate of 0.2 mm/min was applied during the tests. The longitudinal strains of the specimens were measured using an extensometer with a gauge length of 50 mm. The experimental stress–strain curves were replicated using Equations (1) and (2) recommended by Ramberg and Osgood [37] and updated by Hill [38].

$$\varepsilon = \frac{f}{E} + 0.002\left(\frac{f}{f_{0.2}}\right)^n \tag{1}$$

$$n = \frac{\ln 2}{\ln\left(\frac{f_{0.2}}{f_{0.1}}\right)} \tag{2}$$

where ε represents the strain, f is the tensile stress, E denotes the modulus of Elasticity, $f_{0.1}$ and $f_{0.2}$ stand for the 0.1 % and 0.2 % proof stress, respectively and n is the strain hardening parameter. The material properties of the aluminium alloy tubes determined from the tensile tests of coupons are listed in Table 2, where f_u represents the ultimate tensile stress, ε_u is the strain at f_u and ε_f denotes strain related to fracture. The characteristic values of 0.2 % proof stress ($f_{0.2,EC9}$), the ultimate tensile strength ($f_{u,EC9}$) and the strain hardening exponent (n_{EC9}) suggested by Eurocode 9 (EC9) [35] are also provided in Table 2. It can be seen that the values of $f_{0.2}$ and f_u obtained from the experiments are generally higher than the values suggested by Eurocode 9 for 6082-T6 alloy. Fig. 3(c), 3(d) and 3(e) show the dimensions of a typical
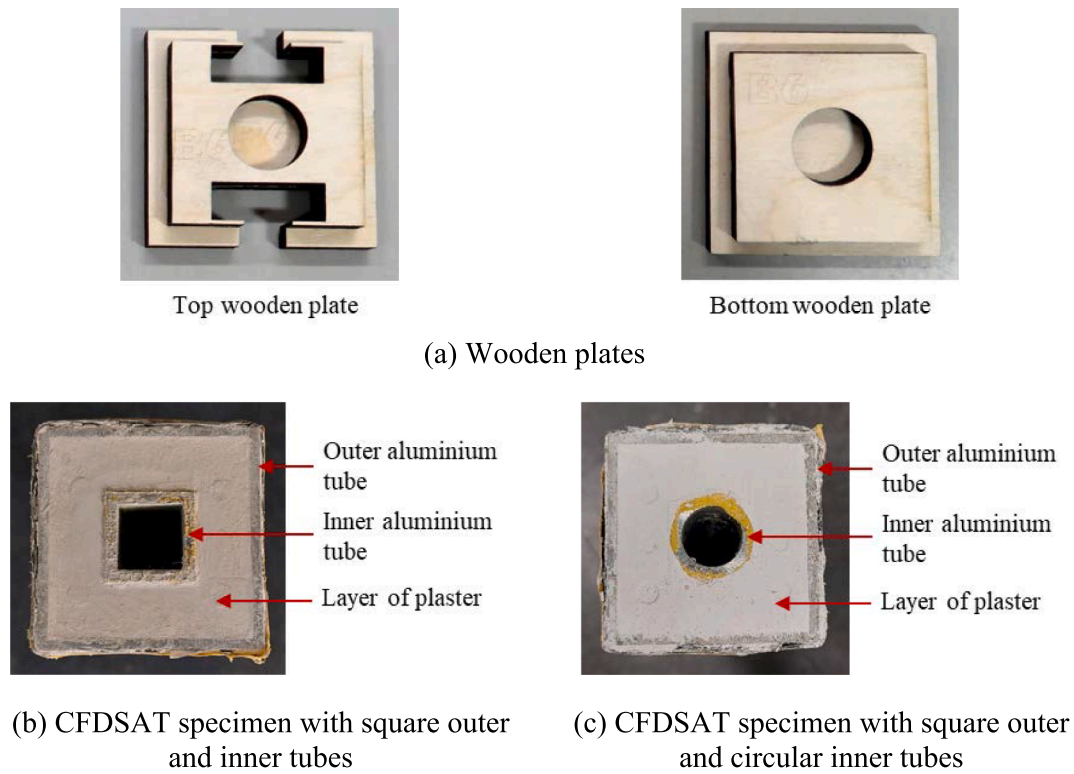
Top wooden plate

Bottom wooden plate

(a) Wooden plates

Outer aluminium tube

Inner aluminium tube

Layer of plaster

(b) CFDSAT specimen with square outer and inner tubes

Outer aluminium tube

Inner aluminium tube

Layer of plaster

(c) CFDSAT specimen with square outer and circular inner tubes

Fig. 2. Photographs of wooden plates and typical cross-sections of CFDSAT specimens.

coupon, typical failure modes of some coupons and typical experimental stress–strain curves of S76.2 × 4.8 and C19.2 × 3.2 material coupons along with the respective Ramberg-Osgood curves, respectively.

2.2.2. Concrete

For preparing the concrete ordinary (Type I) Portland cement, medium coarse silica sand, limestone with a maximum size of 10 mm and normal water were used. These ingredients were mixed by weight at a ratio of 1:1.5:2.5:0.5. Compressive tests of concrete cubes were carried out to determine the material properties of the concrete infill. Four standard cubes with 100 mm × 100 mm × 100 mm nominal size were cast using the same concrete mix of the CFDSAT columns and cured for 28 days. The compressive tests were conducted according to the guidance of BS EN 12390–3 [39] and the test results are reported in Table 3 including the density of the cubes.

2.3. Flexural buckling tests

Axial compression tests were carried out to study the flexural buckling behaviour and determine the ultimate load of CFDSAT specimens. Before the tests, both ends of all specimens were made flat by milling and strengthened with carbon fibre-reinforced polymer (CFRP) to avoid any localised failure at any end [7,30]. Moreover, a plaster layer was employed on the top surface of the infilled concrete of each end to ensure uniform distribution of the axial compressive load [7,30]. The pin-ended boundary condition was created using a steel plate containing deep grooves and a wage plate with a knife edge and applied at both ends of a specimen to allow rotation about the buckling axis. To ensure concentric alignment of the specimens along with the knife edges, a steel channel was loosely bolted using steel plates at each end. A 600 kN hydraulic testing machine was utilised for applying the displacement-control load at a rate of 0.2 mm/min. A load of 2 kN was employed initially to eliminate any gap at the loading point. During the tests, four linear variable differential transducers (LVDTs) were used, in which two were positioned at the mid-length to measure the lateral

displacement and two were placed at the bottom channel to track the rotation of the specimens. Two strain gauges were attached at the mid-height of two faces parallel to the bending axis of a specimen to record the in-plane axial strains. A data logger with eight recording channels was used to record all the data during the tests. At the beginning of the tests, the actual initial loading eccentricity (e_0) was determined based on the observed lateral displacement and strain values to ensure that the initial loading eccentricity was less than $L_e/1000$ [7]. The e_0 was calculated by Equation (3) [7] and listed in Table 4.

$$e_0 = \frac{EI(\varepsilon_{max} - \varepsilon_{min})}{D_o N} - \delta - \omega_g \tag{3}$$

where I represents the second moment of area of the cross-section, N is the axial compressive load, δ is mid-height lateral displacement and ε_{max} and ε_{min} are the maximum and minimum strain values at recorded N, respectively. Fig. 4 presents a photo and a schematic drawing of the test setup.

3. Test results

The failure pattern of all CFDSAT columns was examined and the failure pattern of a typical specimen is presented in Fig. 5. It was observed that the predominant failure pattern of all specimens was flexural buckling (Fig. 5) as the pin-ended set-up allowed the specimens to rotate about the buckling axis. No inward or outward local buckling was identified at the outer tube of the CFDSAT columns. It attributes to the concrete infill which effectively prevented the occurrence of inward local buckling. Moreover, no fracture was noticed in the outer tube of any specimen. To investigate the failure mode of the inner components, the outer tube and concrete infill of typical specimens were partly cut and detached after the tests. The failure pattern of the inner profile and the concrete infill of a typical specimen is presented in Fig. 6(a) and 6(b), respectively. Fig. 6(a) illustrates that, same as the outer tube, the inner tube displayed obvious flexural buckling. However, no inward or outward bulging or fracture was found in the inner tube of the inspected
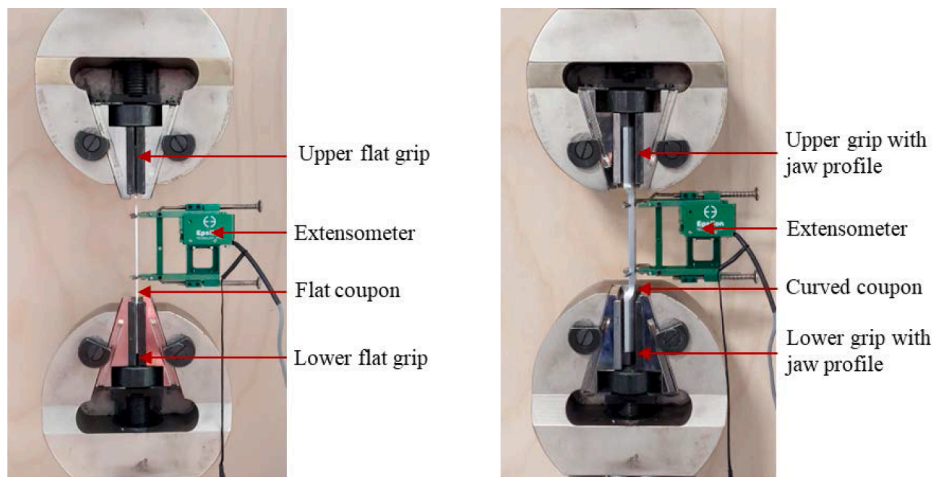
(a) Tensile test of flat coupon
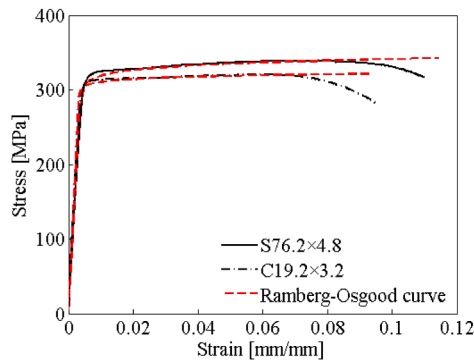
(b) Tensile test of curved coupon
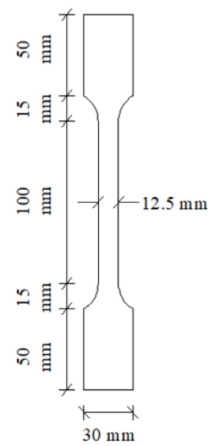
(c) Dimensions of a typical coupon

(d) Typical failure modes of some coupons

(e) Typical stress-strain curves

Fig. 3. Coupon test set-up, dimensions of a typical coupon, typical failure modes of some coupons and typical experimental and corresponding Ramberg-Osgood stress–strain curves.

specimens. It can be seen from Fig. 6(b) that some small horizontal cracks in concrete appeared in the tension region near the mid-height of the specimen as tension stresses are higher in this region.

Fig. 7 presents the applied axial load versus corresponding mid-height lateral displacement curves for all tested specimens. The curves are plotted using the compressive load and lateral displacement data recorded from the load cell of the machine and the LVDT positioned at the mid-length of the specimens, respectively. It is found that initially

the relationship between the axial load and the mid-height lateral displacement is linear which indicates that the materials of the specimens were in the elastic stage. After the elastic stage, all curves diverge from linear to nonlinear response as the growth of load decreases compared to the lateral displacement. This is the evidence of the elastic–plastic stage which exists up to the ultimate load. After reaching the ultimate load, a descending part appears in the curves as the load started to fall gradually with the development of lateral displacement. It can be

Table 2
Material properties of the aluminium hollow section.

Specimen	E (GPa)	$f_{0.1}$ (MPa)	$f_{0.2}$ (MPa)	$f_{0.2,EC9}$ (MPa)	f_u (MPa)	$f_{u,EC9}$ (MPa)	ε_u (%) (mm/mm)	ε_f (%) (mm/mm)	n	n_{EC9}
S19.2 × 1.6	72,500	185	189	160	215	195	4.57	5.45	28.83	24
S25.4 × 1.6	68,700	192	197	250	229	290	6.43	11.40	27.55	32
S25.4 × 3.2	70,000	276	283	250	328	290	7.66	16.00	28.06	32
S50.8 × 3.2	68,300	257	264	250	304	290	7.49	14.70	28.19	32
S63.5 × 3.2	69,900	157	164	250	212	290	6.69	15.60	21.94	32
S76.2 × 4.8	70,700	305	311	250	338	290	5.97	11.70	33.91	32
C19.2 × 3.2	72,800	303	306	160	320	195	5.18	8.94	36.53	24
C25.4 × 3.2	71,900	283	289	250	327	290	8.50	13.00	29.58	32

Table 3
Density and compressive strength of concrete cubes.

Concrete cube	Density (kg/m³)	Compressive strength (MPa)
1	2427	37.2
2	2392	35.7
3	2424	36.8
4	2432	36.5
	Mean	36.5

Table 4
Initial loading eccentricity, failure mode, critical buckling load and ultimate load of CFDSAT specimens.

| Specimen	e_0 (mm)	Failure mode	N_{cr} (kN)	$N_{u,Test}$ (kN)
S50.8 × 3.2-S19.2 × 1.6	0.52	FB	192.17	143.30
S63.4 × 3.2-S19.2 × 1.6	0.89	FB	429.93	179.83
S63.4 × 3.2-S25.4 × 3.2	0.68	FB	437.68	216.85
S76.2 × 4.8-S19.2 × 1.6	0.81	FB	980.77	464.47
S76.2 × 4.8-S25.4 × 1.6	0.93	FB	978.74	455.64
S76.2 × 4.8-S25.4 × 3.2	0.66	FB	988.00	466.51
S63.4 × 3.2-C19.2 × 3.2	0.64	FB	434.63	210.67
S63.4 × 3.2-C25.4 × 3.2	0.60	FB	435.56	198.51
Note: FB = Flexural buckling				

observed from the figure that a certain ductility is visible in all curves, attributed to the beneficial composite action of the three elements of the CFDSAT specimens. The ultimate load ($N_{u,Test}$) of all specimens determined from the tests is listed in Table 4 including their critical buckling load (N_{cr}) (see Equation (9) in Section 5.1). It is found from the table that the ultimate load of the CFDSAT specimens improved noticeably by increasing the dimensions of outer tube when the dimensions of inner tube are constant. For example, the ultimate load of the specimen S50.8 × 3.2-S19.2 × 1.6 improved by 25.5 % compared to the specimen S63.4 × 3.2-S19.2 × 1.6 as the outer dimension of outer tube of the later is increased from 50.8 mm to 63.4 mm. Moreover, it is observed that the ultimate load of the CFDSAT specimens decreased with the increase of the depth/diameter of inner tube when the outer tube dimensions are constant. This is because the area of concrete infill is decreased, resulting in the reduction of cross-sectional resistance. For example, when the outer diameter of the inner tube is increased from 19.2 mm to 25.4 mm, the ultimate load of the specimen S63.4 × 3.2-C19.2 × 3.2 is reduced approximately by 5.5 % compared to the capacity of the specimen S63.4 × 3.2-C25.4 × 3.2. The influence of the dimensions of outer and inner tubes on the ultimate load of the specimens is further studied by the FE analysis and discussed in Section 4.3.

4. Finite element (FE) analysis

In this study, ABAQUS software [40] was used to perform the FE analysis of the buckling behaviour of CFDSAT columns. Non-linear FE models of the CFDSAT specimens were developed and their accuracy was evaluated by comparing the FE results with those obtained from the experiments. A numerical parametric investigation was subsequently carried out.
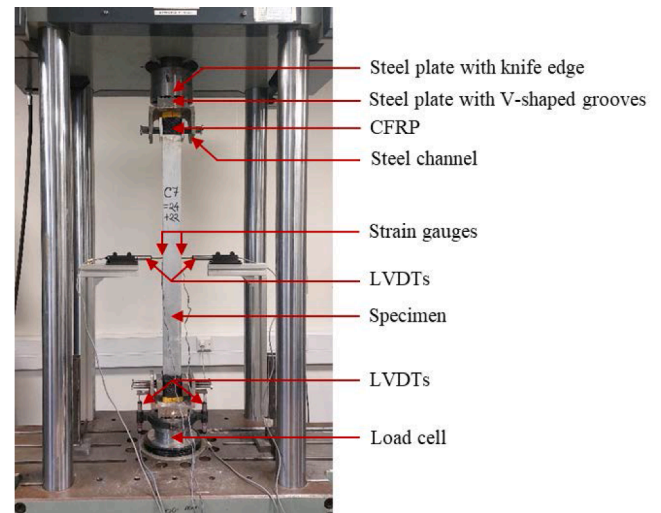

(a) Photograph
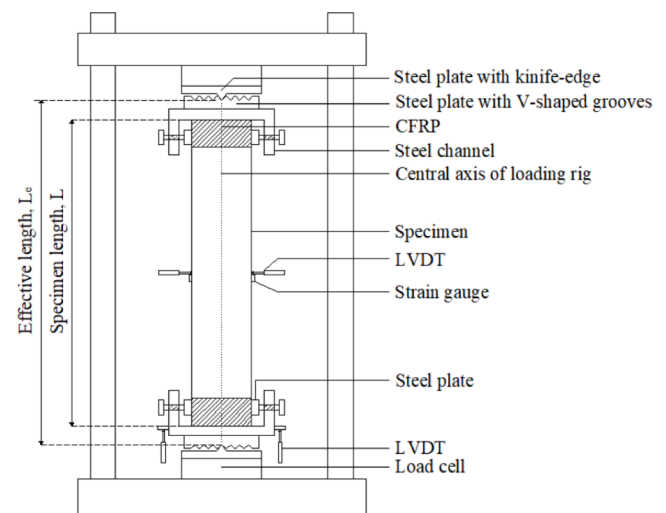
(b) Schematic diagram

Fig. 4. Photograph and schematic diagram of the axial compression test setup.

4.1. FE modelling

All CFDSAT specimens were modelled using the measured dimensions of the cross-sections and material properties listed in Tables 1, 2 and 3. Eight-node hexahedral solid elements with reduced integration (C3D8R) were applied to simulate the hollow tubes and the concrete infill [7]. A mesh sensitivity investigation was carried out for choosing the optimum size of the C3D8R elements. It was found that 5 mm element size is suitable for achieving accurate results in a reasonable
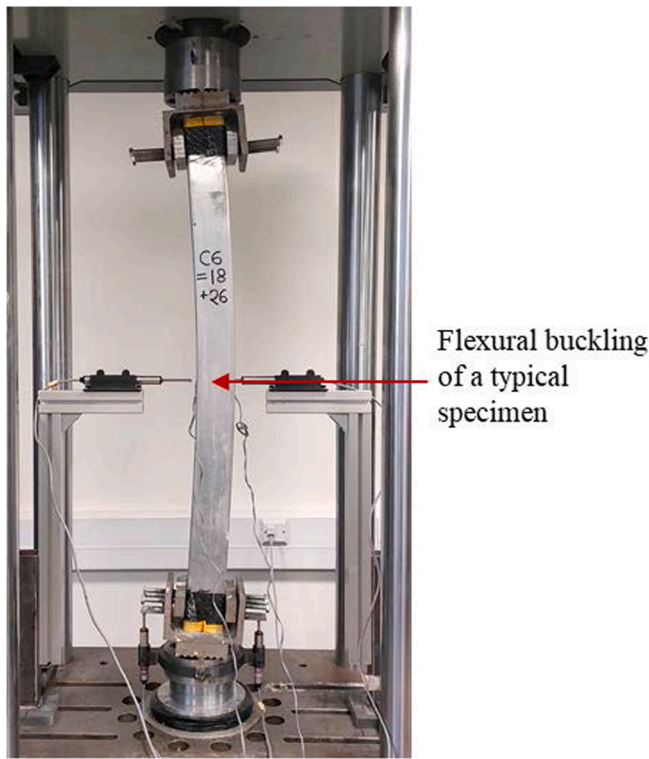
Fig. 5. Flexural buckling of a typical CFDSAT specimen S76.2 × 4.8-S25.4 × 3.2.

time. Thus, 5 mm element size was adopted for the concrete and the hollow tubes by using the structured meshing approach. The thickness of outer and inner hollow sections was discretised at least into three elements to obtain the nonlinear behaviour of the thin-walled sections [41].

For simulating the properties of hollow sections, the elastic–plastic model based on the von Mises yield principle with isotropic hardening was considered. The modulus of Elasticity of aluminium alloy reported in Table 2 and Poisson's ratio of 0.33 was used for the elastic response. According to ABAQUS software's guidelines, the nominal stress-plastic

strain data were inputted by converting them to true stress-logarithmic plastic strain data for modelling the plastic behaviour. The inbuilt concrete damage plasticity (CDP) model was used to replicate the material properties of concrete. The modulus of Elasticity of concrete was calculated using the formula provided in Eurocode 4 [34] and the value of Poisson's ratio was considered as 0.2. In the CDP model, the dilation angle value of 40° was used [42], while the default values of 0.1 and 0 were applied for the flow potential eccentricity and the viscosity parameter, respectively. The ratio of the compressive strength due to biaxial loading over uniaxial compressive strength was defined based on the formula recommended by Papanikolaou and Kappos [43] and the compressive meridian was determined according to the suggestion given by Yu et al. [44]. The confined concrete model proposed by Tao et al. [42] (Fig. 8) is a well-known constitutive model to capture the compressive behaviour of confined concrete. This model was developed and calibrated for the concrete-filled steel tubular sections. Therefore, its application is limited to the concrete confined by a single skin metal section. To apply this model for the concrete confined by double skin metal tubes a modified confinement factor is proposed in the previous studies [18,19,21,45]. In this study, this model with the modified confinement factor is adopted to simulate the compressive response of the concrete of CFDSAT columns. The response of concrete infill subjected to tensile force was considered by a linear relationship of stress–strain up to 10 % of concrete compressive strength and a post-peak branch based on fracture energy [46–48].

The built-in surface-to-surface contact option in ABAQUS was applied to mimic the interaction between the concrete infill and the aluminium hollow tubes. The outer faces of the concrete were set as the master surfaces, while the outer faces of the inner section and the inner faces of the outer section were assigned as the slave surfaces. In the vertical direction of the master and the slave surfaces, hard contact was applied for permitting separation under tension and avoiding penetration under compression. Coulomb friction with a coefficient of 0.3 was employed in the lateral direction of the two types of surfaces for allowing sliding [7].

The residual stresses generated during the production of aluminium alloy are very low [49]. The impact of initial local geometric imperfection on the buckling behaviour of CFDSAT columns is not significant as the sensitivity of the hollow sections to the local buckling is reduced due to the existence of concrete infill. Hence, the effects of residual
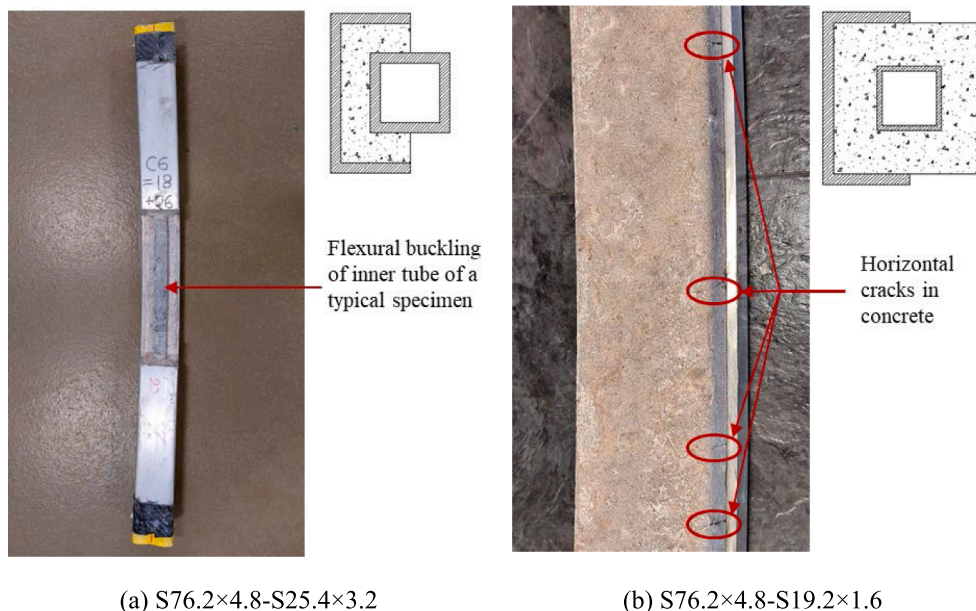

(a) S76.2×4.8-S25.4×3.2

(b) S76.2×4.8-S19.2×1.6

Fig. 6. Failure pattern of (a) the inner tube of a typical CFDSAT specimen, (b) the concrete infill of a typical CFDSAT specimen.

(a) S50.8×3.2-S19.2×1.6

(b) S63.4×3.2-S19.2×1.6

(c) S63.4×3.2-S25.4×3.2

(d) S76.2×4.8-S19.2×1.6

(e) S76.2×4.8-S25.4×1.6

(f) S76.2×4.8-S25.4×3.2

(g) S63.4×3.2-C19.2×3.2
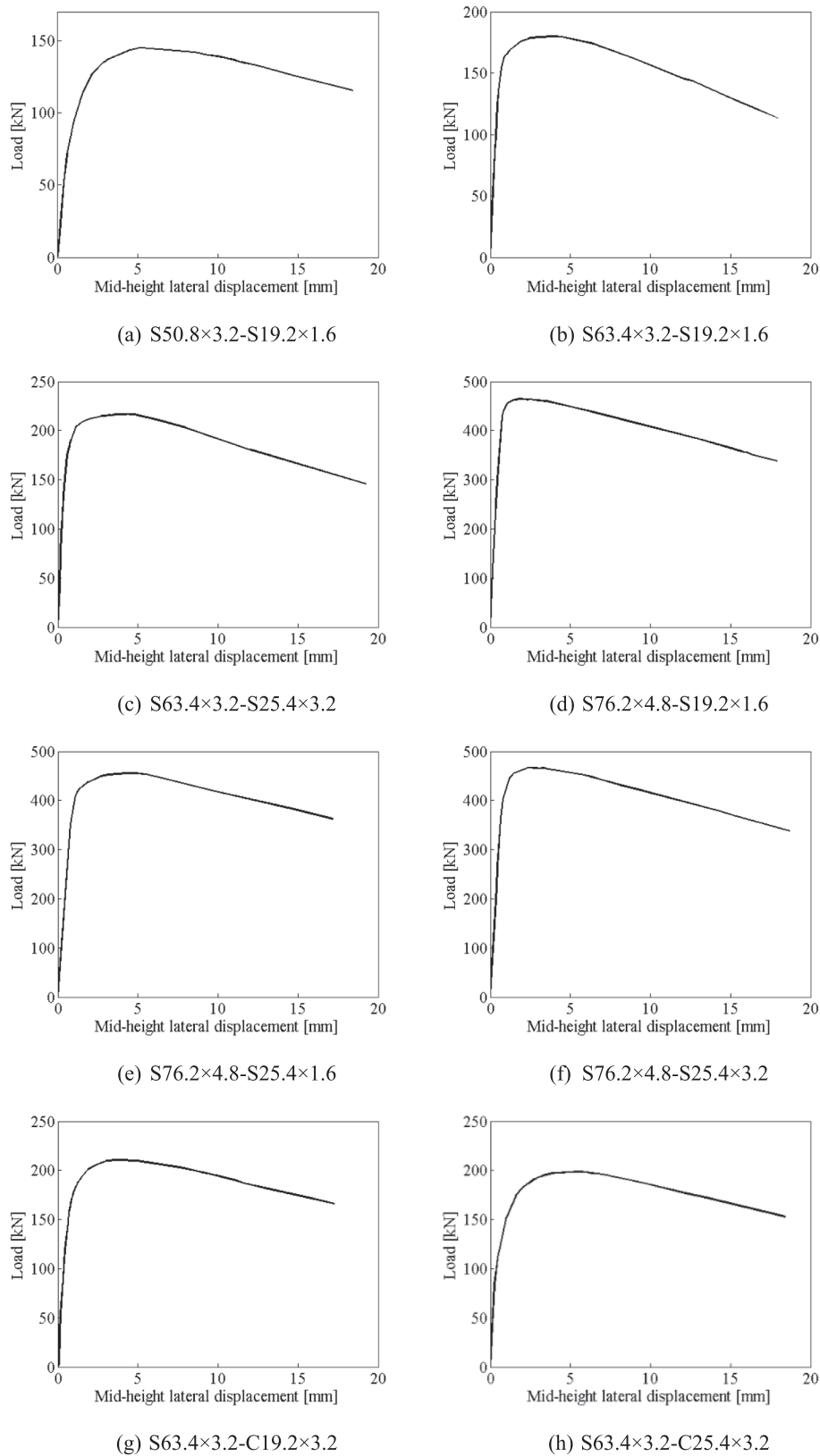
(h) S63.4×3.2-C25.4×3.2

Fig. 7. Axial load versus mid-height lateral displacement curves of the CFDSAT specimens.

stresses and initial local geometric imperfections were not included in the FE modelling [7]. The effect of initial global imperfection was considered in the non-linear FE analysis by integrating the lowest global buckling mode determined from an eigenvalue buckling analysis. The

amplitude of the global imperfection of a specimen was calculated by adding the value of ω_g reported in Table 1 with the respective value of e_0 mentioned in Table 4. The pin-ended supports were simulated by applying the boundary conditions on the reference points which were
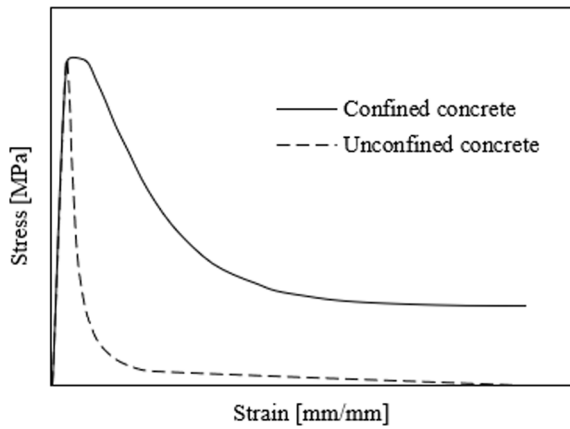
Fig. 8. Compressive behaviour of confined concrete [42].

created on the centroid of the top and bottom ends of the specimens. The distance between the two reference points was the same as the effective length of the specimens. It was assumed that the top reference point can move along the longitudinal direction of the specimen (Z direction) and both reference points can rotate around the buckling axis (X direction), as shown in Fig. 9(a). Due to simplicity, the CFRP warps were not modelled in this study, however, potential local failures at the ends were prevented by applying the coupling constraints between each reference point and each end of the specimens [7,50]. At the top reference point, the axial compressive load was employed using a displacement control approach. Fig. 9 shows the geometry, loading direction, boundary conditions and cross-section of a typical FE model.

4.2. FE model validation

The accuracy of the developed FE model was determined by comparing the FE ultimate load, flexural rigidity, load versus mid-height lateral displacement curve and failure mode with the corresponding test results. An imperfection sensitivity investigation was carried out to evaluate an appropriate global imperfection amplitude for using in the numerical parametric study. In this study, four different global imperfection values were considered, i.e., the measured value (i.e., summation of ω_g and e_0) and three values of fractions of the effective length, i.e., $L_e/1000$, $L_e/1500$ and $L_e/2000$. Table 5 reports the ratios of FE over test ultimate load ($N_{u,FE}/N_{u,Test}$) for the four global imperfection amplitudes and FE over test flexural rigidity ($EI_{e,FE}/EI_{e,Test}$) for $L_e/1000$. It can be found that the global imperfection value of $L_e/1000$ offers an excellent prediction of the ultimate load with a mean value of $N_{u,FE}/N_{u,Test}$ 1.02 and the corresponding coefficient of variation (COV) of 0.04. Moreover, the flexural rigidity values of the specimens obtained from the tests are

Table 5
Ratios of FE over test ultimate load and flexural rigidity.

Specimen	$N_{u,FE}/N_{u,Test}$				$EI_{e,FE}/EI_{e,Test}$
	Global imperfection value				
	Measured	$L_e/1000$	$L_e/1500$	$L_e/2000$	$L_e/1000$
S50.8 × 3.2-S19.2 × 1.6	1.04	1.00	1.07	1.11	1.01
S63.4 × 3.2-S19.2 × 1.6	1.09	1.10	1.14	1.15	1.06
S63.4 × 3.2-S25.4 × 3.2	0.98	0.99	1.03	1.05	0.97
S76.2 × 4.8-S19.2 × 1.6	1.02	1.02	1.04	1.05	0.98
S76.2 × 4.8-S25.4 × 1.6	1.02	1.03	1.06	1.07	1.08
S76.2 × 4.8-S25.4 × 3.2	1.07	1.04	1.07	1.08	1.03
S63.4 × 3.2-C19.2 × 3.2	0.98	0.96	0.99	1.00	0.99
S63.4 × 3.2-C25.4 × 3.2	1.02	1.01	1.04	1.07	1.02
Mean	1.03	1.02	1.05	1.07	1.02
COV	0.03	0.04	0.04	0.04	0.03

Axial load
Inner aluminium tube
Concrete infill
BC at top:
$u_x = u_y = 0$, $u_z \neq 0$
$u_{ry} = u_{rz} = 0$, $u_{rx} \neq 0$

Outer aluminium tube

BC at bottom:
$u_x = u_y = u_z = 0$
$u_{ry} = u_{rz} = 0$, $u_{rx} \neq 0$

(a)

Outer aluminium tube
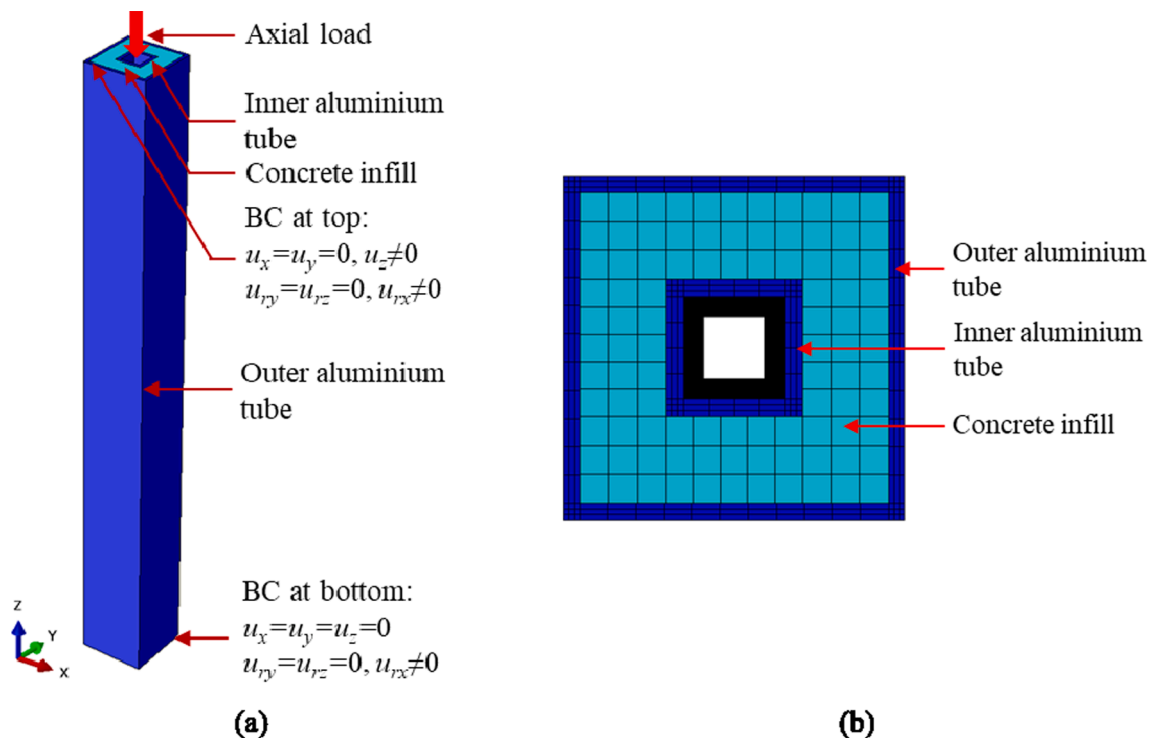Inner aluminium tube
Concrete infill

(b)

Fig. 9. (a) Loading direction and boundary conditions, (b) cross-section of a typical FE model.

very close to the ones of the FE analyses suggesting a very good accuracy of the developed models. Fig. 10 presents the comparison between the FE (for $L_e/1000$) and test axial load versus mid-height lateral displacement graphs of two specimens. The figure illustrates that the developed model accurately simulates the axial load versus mid-height lateral displacement relationship of the specimens. Moreover, Fig. 11 demonstrates a good agreement between the failure mode observed from the test and the FE analysis of a typical specimen. From the above comparisons, it can be concluded that the developed FE model accurately replicates the structural response of CFDSAT columns.

4.3. Parametric study

Using the developed model, a numerical parametric investigation was performed to study the influence of hollow ratio, member slenderness, cross-section slenderness of hollow tubes and concrete strength on the ultimate load of CFDSAT columns. The stress–strain curves of the materials of CFDSAT cross-sections presented in Fig. 12 were used in the parametric study. In total 81 CFDSAT columns were modelled considering different outer sections, i.e., 45×45, 60×60, 75×75, 100×100, 120×120 and 150×150 mm^2 with wall thickness varied from 1 to 8 mm and inner sections, i.e., 20×20, 25×25, 30×30 and 35×35 mm^2 with wall thickness ranged from 1 to 5 mm. Two combinations of outer and inner cross-section shapes, i.e., square-square and square-circular, three different member heights, i.e., 500, 1000 and 1500 mm and three different concrete cube compressive strengths, i.e., 30, 40 and 50 MPa were chosen.

4.3.1. Effect of hollow ratio

To investigate the influence of hollow ratio on the ultimate load of CFDSAT columns a wide range of depth/diameter of the outer and the inner cross-sections was considered in this study. The hollow ratio is calculated using Equation (4).

$$\alpha = \frac{D_i}{D_o - 2t_o} \tag{4}$$

where α is the hollow ratio which is varied from 0.14 to 0.86 by changing the depth/diameter of outer and inner hollow sections. The effect of α on the axial load versus mid-length lateral displacement graphs of typical CFDSAT columns having constant length and concrete strength is illustrated in Fig. 13. It can be found from Fig. 13(a) that the ultimate load of CFDSAT columns significantly improved with the decrease of α (i.e., increase of depth of the outer tube) when the inner section's dimensions remain the same. This is related to the fact that by increasing the depth, the flexural rigidity of the outer profile increases along with the increase of concrete area, which contributes to the improvement of the ultimate load of the specimens. Fig. 13(b) demonstrates that when the dimensions of the outer tube are constant the ultimate load of CFDSAT columns decreased slightly by enlarging the

depth/diameter of the inner section (i.e., increase of α). These observations can be further explained by Fig. 14, which shows the contribution of the outer tube, concrete infill and inner profile to the ultimate load of typical CFDSAT specimens. It can be observed from Fig. 14(a) and (b) that the outer profile has the largest contribution to the overall capacity, followed by the concrete infill which provides the second-highest cross-sectional resistance to axial compression among the three components, thereby justifying the increase in the ultimate load noticed in Fig. 13(a). The contribution of the inner profile to the cross-sectional compressive resistance is the lowest compared to the other components of CFDSAT columns. Therefore, the variation of the depth/diameter of the inner profile has negligible influence on the ultimate load of CFDSAT columns.

4.3.2. Effect of depth to thickness ratio of the outer tube

Fig. 15 presents the effect of depth to thickness ratio of the outer tube (D_o/t_o) on the axial load versus mid-length lateral displacement of typical CFDSAT columns with the same length and concrete strength. The D_o/t_o ratio ranging from 6 to 150 was considered by altering the outer section thickness. It is observed from the figure that the effect of D_o/t_o ratio is remarkable on the buckling behaviour of CFDSAT columns, as the ultimate load of the columns increased noticeably by decreasing D_o/t_o ratio (i.e., increase of thickness of outer tube). This is because the larger thickness provides higher flexural rigidity of the outer tube, which results in an improved ultimate load of the specimens. Similar observation was noticed for the other studied specimens having lower D_o/t_o ratio.

4.3.3. Effect of depth/diameter to thickness ratio of the inner tube

Fig. 16 illustrates the influence of the depth/diameter to thickness ratio of the inner section (D_i/t_i) on the buckling behaviour of CFDSAT columns having constant length and concrete strength. The D_i/t_i ratios were considered from 4 to 35 by varying the thickness of square and circular inner sections. Fig. 16 indicates that with the decrease of D_i/t_i ratio the ultimate load of the CFDSAT columns generally improved, as the smaller D_i/t_i ratio means larger thickness of the inner profile which offers an addition in the ultimate load of the specimens. However, the strength increase of D_i/t_i is minimal, as the inner tube provides the lowest cross-sectional resistance among the three components of the CFDSAT columns (see Fig. 14).

4.3.4. Effect of member slenderness ($\bar{\lambda}$)

To examine the effect of member slenderness ($\bar{\lambda}$) on the capacity of CFDSAT columns, three different column lengths, i.e., 500, 1000 and 1500 mm were considered without changing the cross-sectional dimensions of the specimens and concrete strength. The member slenderness is determined according to Eurocode 4 [34] (see Equation (8) in Section 5.1). Fig. 17 illustrates the influence of $\bar{\lambda}$ on the axial load versus mid-length lateral displacement graphs of a typical CFDSAT specimen.
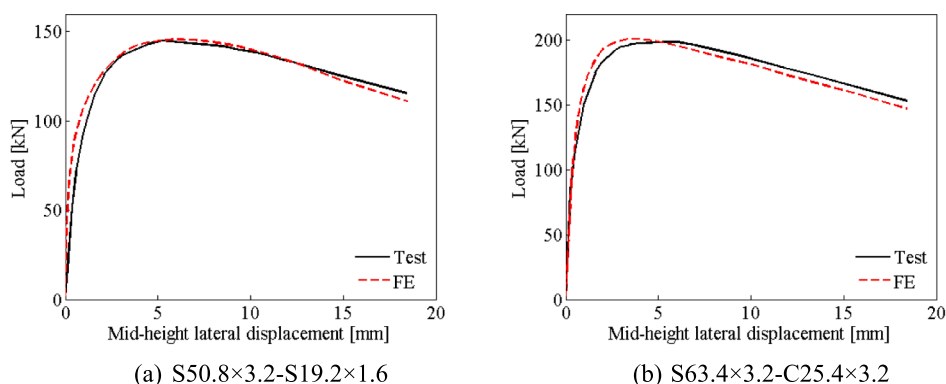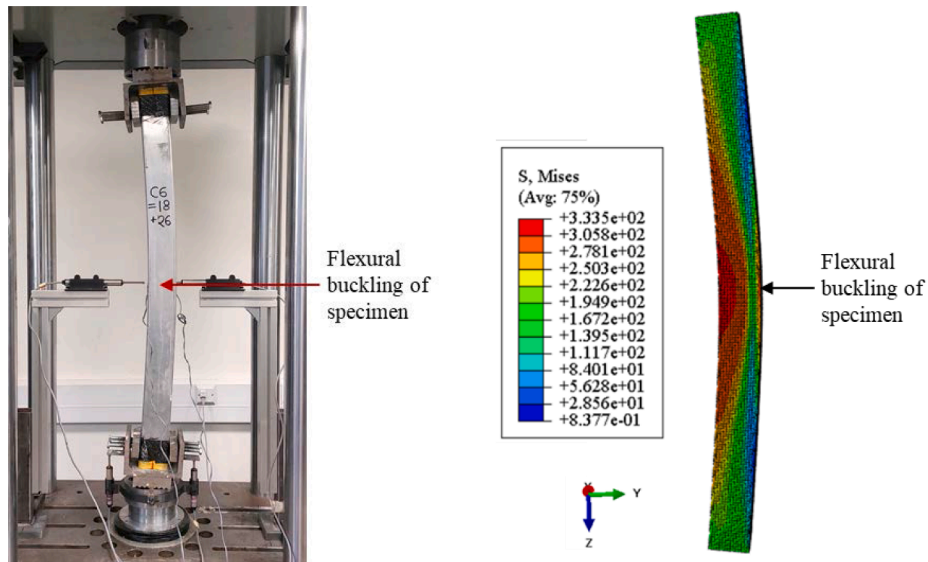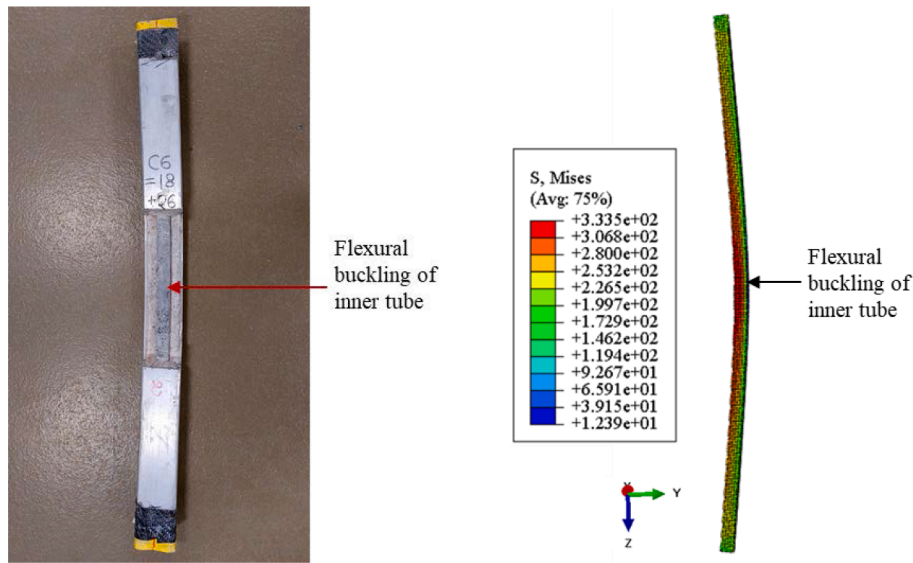

(a) S50.8×3.2-S19.2×1.6

(b) S63.4×3.2-C25.4×3.2

Fig. 10. Comparison of test and FE axial load versus mid-height lateral displacement curves.
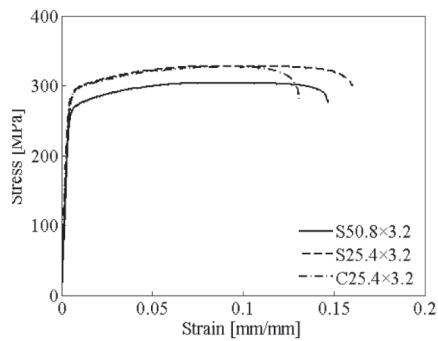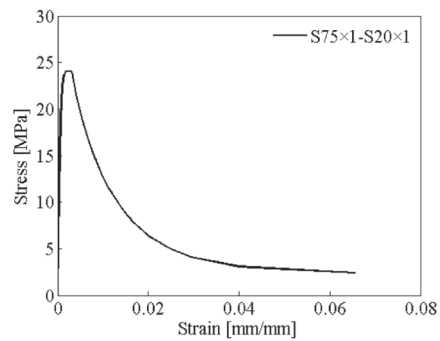
(a) Flexural buckling of S76.2×4.8-S25.4×3.2

(b) Flexural buckling of inner tube of S76.2×4.8-S25.4×3.2

Fig. 11. Comparison of test and FE failure modes of a typical CFDSAT specimen.

(a) Stress-strain curves of aluminium alloy sections

(b) Typical compressive stress-strain curve of confined concrete

Fig. 12. Stress–strain curves of the materials of CFDSAT cross-sections used in the parametric study.

(a) CFDSAT specimens with constant
inner tube (S20×1)

(b) CFDSAT specimens with constant
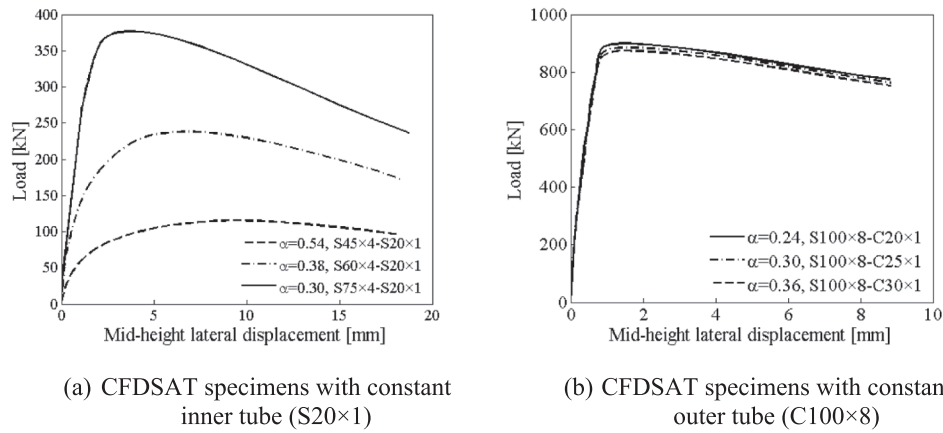outer tube (C100×8)

Fig. 13. Effect of hollow ratio on the axial load versus mid-height lateral displacement of typical CFDSAT specimens having constant length and concrete strength.
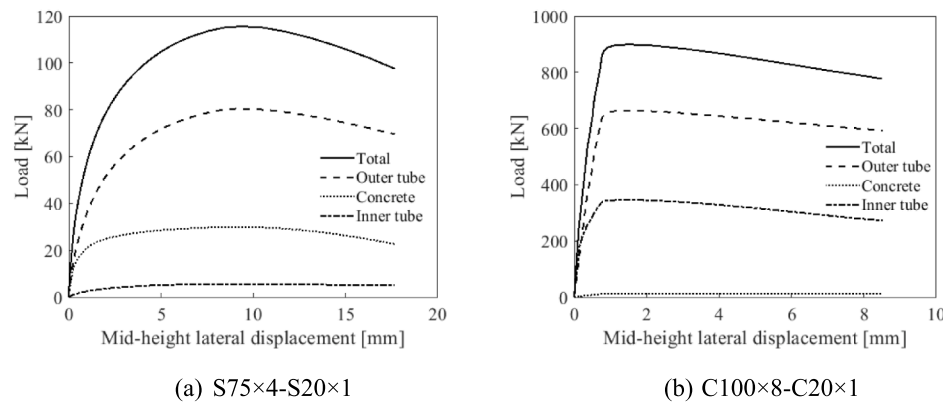

(a) S75×4-S20×1

(b) C100×8-C20×1

Fig. 14. Contribution of the outer tube, concrete infill and inner tube on the ultimate load of typical CFDSAT specimens.
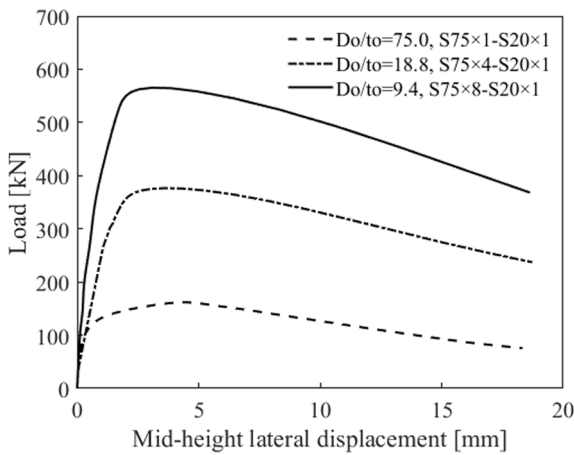

Fig. 15. Effect of D_o/t_o ratio on the axial load versus mid-height lateral displacement curves of typical CFDSAT specimens having constant length and concrete strength.

Fig. 16. Effect of D_i/t_i ratio on the axial load versus mid-height lateral displacement curves of typical CFDSAT specimens having constant length and concrete strength.

The figure illustrates that by increasing $\bar{\lambda}$ (i.e., larger member length) the ultimate load of CFDSAT columns reduced noticeably. This can be clarified by the fact that when the cross-sectional dimensions of the specimens are constant, the critical buckling load of columns decreases with the increase of the member length, which makes the columns prone to global buckling failure, resulting in a reduced ultimate load. More-over, it can be observed from Fig. 17 that the curves of columns with lower $\bar{\lambda}$ exhibit a sharp drop in load after reaching the ultimate capacity.
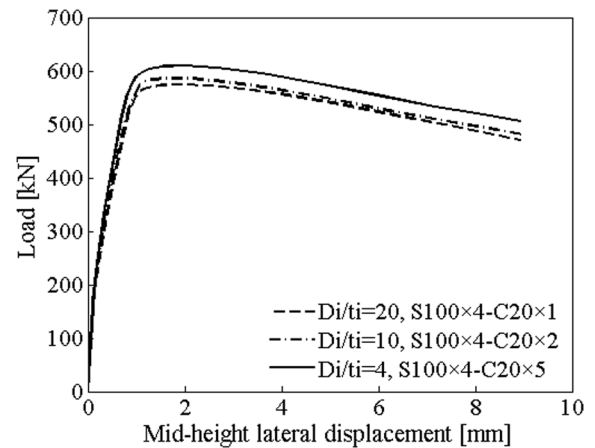
Similar observation is presented in a previous research article on the behaviour of short and slender CFDSST columns [29].

4.3.5. Effect of concrete compressive strength
In the parametric study, three concrete cube compressive strengths (f_{cu}), i.e., 30, 40 and 50 MPa were adopted to investigate the influence of concrete strengths on the ultimate load of CFDSAT columns. The effect of different concrete strengths on the axial load versus mid-height lateral
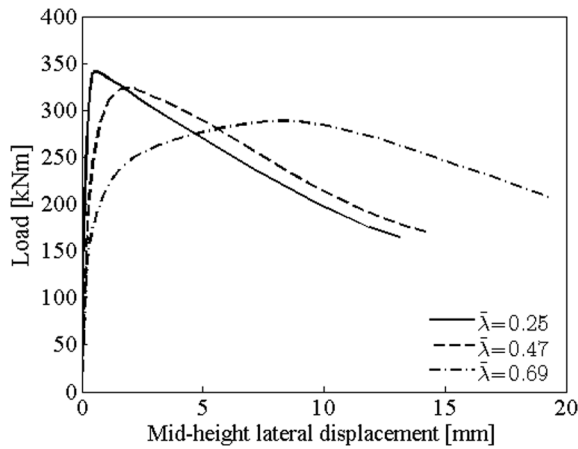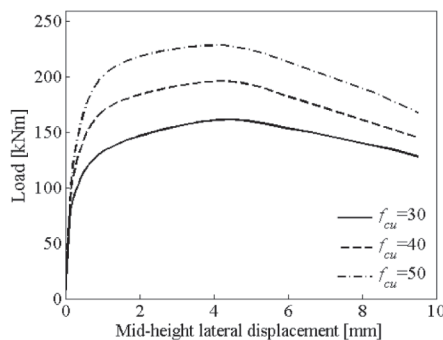
Fig. 17. Effect of member slenderness ($\bar{\lambda}$) on the axial load versus mid-height lateral displacement curves of a typical CFDSAT specimen S100 × 1.5-C20 × 1.

displacement of typical CFDSAT columns having same length is shown in Fig. 18. It can be observed from the figure that the concrete grade has a profound influence on the buckling response of the CFDSAT columns, as the bearing capacity of the columns enhanced substantially with the increase of the compressive strength of concrete. This is related to the fact that concrete provides the second highest cross-sectional resistance among the three components of the CFDSAT columns (see Fig. 14) and improves the ultimate load of the outer tube by preventing the occurrence of inward buckling and slowing down the formation of outward buckling. Hence, the higher grade of concrete adds more cross-sectional resistance and offers stronger support against the local buckling of the outer profile. Moreover, it is also found that the improvement of ultimate capacity due to higher concrete grade is higher for the columns with bigger cross-sections than the smaller ones. For example, the ultimate load of the specimen S75 × 1-S20 × 1 increased by around 41 % for 50 MPa concrete with respect to the 30 MPa ones (Fig. 18(a)), whereas the value is more than 58 % for the specimen S150 × 1-C20 × 1 (Fig. 18 (b)) which is the highest percentage ultimate load increase recorded among the investigated specimens in this study. It indicates that the bigger cross-section contains a larger concrete area which provides more cross-sectional resistance against the axial compression for higher concrete grades.

5. Design recommendations

The existing design code for composite structural members, i.e., Eurocode 4 [34] provides rules for the design of fully concrete-filled carbon steel tubular columns. However, no design rules are available
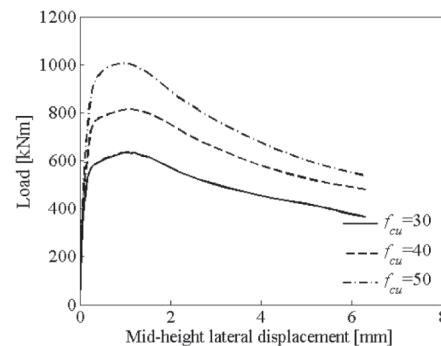
for the design of CFDSAT members [51]. Hence, in this study, a design methodology with a design buckling curve is proposed based on the Eurocode 4 [34] framework for determining the capacity of CFDSAT columns. The accuracy of the proposed methodology is assessed by comparing the design strengths with the corresponding test and FE data. It should be noted that in the proposed methodology the material partial safety factors were considered equal to unity.

5.1. Design methodology for CFDSAT columns based on Eurocode 4 [34]

In Eurocode 4 [34], a design formula for determining the ultimate load of fully concrete-filled carbon steel structural columns is provided by summing the plastic cross-sectional resistance of the outer tube and the concrete infill. To determine the ultimate load of CFDSAT columns, the formula is modified by substituting the material properties of carbon steel for the outer tube with those of aluminium alloy and considering the contribution of the inner tube by adding its plastic cross-sectional resistance. Thus, the ultimate load of CFDSAT columns is calculated using Equation (5).

$$N_{pl} = A_o f_{0.2,o} + \alpha A_c f_c + A_i f_{0.2,i} \tag{5}$$

where A_o, A_c, and A_i are the cross-sectional areas of the outer section, concrete infill and inner section, respectively. $f_{0.2,o}$ and $f_{0.2,i}$ are the yield (0.2 % proof) stresses of the outer and the inner sections, respectively. f_c is the compressive cylinder strength of concrete, which is considered 80 % of f_{cu}. It is assumed that the concrete reaches its full f_c due to the confinement provided by the outer and inner sections. Therefore, the concrete coefficient α is considered 1 instead of 0.85 [19].

The design strength of the CFDSAT section is converted to member strength by employing a reduction factor χ recommended by Eurocode 4 [34].

$$N_{u,prop} = \chi N_{pl} \tag{6}$$

The expression of χ is given in Equation (7).

$$\chi = \left[\varphi + \sqrt{\phi^2 - \bar{\lambda}^2} \right]^{-1} \leqslant 1.0 \tag{7}$$

In the above equation, φ is a parameter and $\bar{\lambda}$ is the member slenderness. The $\bar{\lambda}$ is calculated by Equation (8).

$$\bar{\lambda} = \sqrt{N_{pl}/N_{cr}} \tag{8}$$

The N_{cr} denotes the critical buckling load or Euler's critical load, which is defined by Equation (9).

$$N_{cr} = \pi^2 EI_e/L_e^2 \tag{9}$$

(a) S75×1-S20×1

(b) S150×1-C20×1

Fig. 18. Effect of concrete cube compressive strength on the axial load versus mid-height lateral displacement curves of a typical CFDSAT specimen having constant length.

where EI_e represents the effective flexural rigidity of the composite section, which is calculated by Equation (10).

$$EI_e = E_o I_o + k_e E_c I_c + E_i I_i \tag{10}$$

where E_o, E_c, and E_i are the modulus of Elasticity of the outer tube, concrete infill and inner tube, respectively. I_o, I_c, and I_i are the moment of inertia of the cross-section of the outer profile, concrete infill and inner profile, respectively. The symbol k_e represents the correction factor which is used to reduce the gross flexural rigidity of the concrete. The value of k_e is taken as 0.6 according to Eurocode 4 [34].

The φ is determined by Equation (11).

$$\varphi = 0.5\left[1 + \alpha_1(\bar{\lambda} - \bar{\lambda_0}) + \bar{\lambda}^2\right] \tag{11}$$

in which, α_1 is the imperfection factor and $\bar{\lambda_0}$ is the limit of the horizontal plateau. The value of α_1 is taken equal to 0.34 which is suggested by Eurocode 4 [34] for composite columns having a ratio of the cross-sectional area of the hollow tube over concrete infill greater than 3 %. The value of $\bar{\lambda_0}$ is considered as 0.1 according to the recommendation provided by Eurocode 9 [35] for Class A materials. It should be noted that in Eurocode 9 [35] the aluminium alloys are categorized into two material classes, i.e., Class A and B and the 6082-T6 aluminium alloy used in this study is a Class A material. Fig. 19 shows the test and FE ultimate load normalised by plastic capacity (i.e., N_u/N_{pl}) against the member slenderness $\bar{\lambda}$. Moreover, the proposed design buckling curve considering the above-mentioned values of α_1 and $\bar{\lambda_0}$ is also presented in the same figure. From the figure, an anticipated decreasing trend of the normalised load can be observed with the increase of the member slenderness $\bar{\lambda}$. It is found that most of the test and the FE data are above the buckling curve, which implies that the proposed design curve is suitable for the CFDSAT columns design and provides safe capacity predictions.
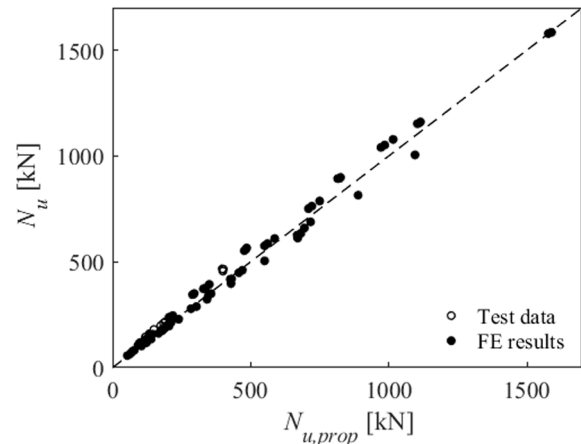
5.2. Ultimate load prediction for CFDSAT columns

To assess the applicability of the proposed design methodology, the predicted ultimate capacities are compared with the corresponding ones obtained from the tests and FE analyses. Table 6 lists the ratios of test and FE ultimate load over the predicted design capacity ($N_u/N_{u,prop}$) along with the corresponding mean and COV values. The mean and COV values of $N_u/N_{u,prop}$ are 1.06 and 0.08, respectively, indicating that the proposed methodology is appropriate to predict the ultimate load of CFDSAT columns. In Fig. 20, the test and FE ultimate load are plotted against the predicted design capacity. It also illustrates the accuracy of the proposed methodology as most of the data in the figure are close to the diagonal line of $N_u = N_{u,prop}$. Overall, it can be summarized that the proposed design methodology can accurately predict the ultimate load

Fig. 19. Proposed design buckling curve for CFDSAT columns.

Table 6
Comparison of the design capacity and effective flexural rigidity of the specimens with the corresponding test and FE values.

|	Specimen	No	$N_u/N_{u,prop}$	$EI_{e,Test/FE}/EI_{e,EC4}$ ($k_e = 0.6$)	$EI_{e,Test/FE}/EI_{e,EC4}$ ($k_e = 1$)
Test	S50.8 × 3.2-S19.2 × 1.6	1	1.22	1.31	1.10
	S63.4 × 3.2-S19.2 × 1.6	1	1.20	1.30	1.06
	S63.4 × 3.2-S25.4 × 3.2	1	1.13	1.22	1.01
	S76.2 × 4.8-S19.2 × 1.6	1	1.16	1.21	1.03
	S76.2 × 4.8-S25.4 × 1.6	1	1.14	1.20	1.02
	S76.2 × 4.8-S25.4 × 3.2	1	1.17	1.28	1.08
	S63.4 × 3.2-C19.2 × 3.2	1	1.14	1.34	1.09
	S63.4 × 3.2-C25.4 × 3.2	1	1.14	1.33	1.08
	FE (mean)	81	1.05	1.41	1.06
	Mean (all)		1.06	1.40	1.05
	COV (all)		0.08	0.13	0.07

Fig. 20. Comparison of the design capacity with the corresponding test and FE ultimate load.

of CFDSAT columns.

5.3. Assessment of Eurocode 4 [34] concrete correction factor

In order to evaluate the suitability of applying Eurocode 4 [34] concrete correction factor ($k_e = 0.6$) for determining the effective flexural rigidity of CFDSAT columns, the effective flexural rigidities of the specimens calculated from test and FE data ($EI_{e,Test/FE}$) are compared with the values predicted according to Eurocode 4 ($EI_{e,EC4}$) (see Equation (10) in Section 5.1). The ratios of $EI_{e,Test/FE}$ over $EI_{e,EC4}$ are reported in Table 6, including their mean and COV values, which are 1.40 and 0.13, respectively. The high mean value can be related to the reduced flexural rigidity of concrete, which is 60 % of concrete gross flexural rigidity and leads to conservative design predictions for CFDSAT columns. Aiming to improve the accuracy of this formula and make it applicable to CFDSAT columns, the concrete correction factor k_e is set equal to 1, assuming that the concrete in the CFDSAT section can achieve its full flexural rigidity because of the confinement provided by the outer and inner tubes. The ratios of $EI_{e,Test/FE}/EI_{e,EC4}$ considering $k_e = 1$ are also listed in Table 6. It can be seen that by considering the full flexural rigidity of concrete, the
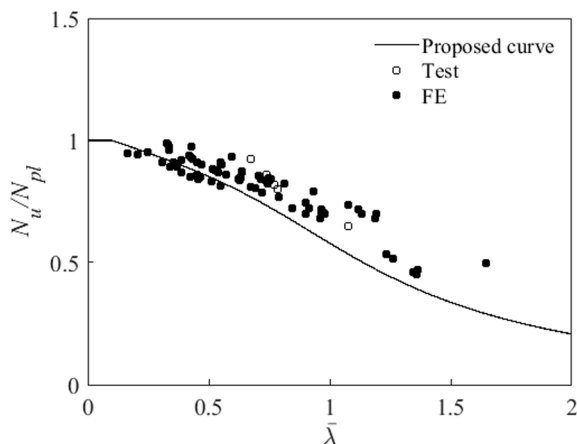
accuracy of the flexural rigidity formula for CFDSAT columns is improved by 35 %. Fig. 21 presents the test and FE effective flexural rigidities ($EI_{e,Test/FE}$) of the specimens against the predicted values ($EI_{e,EC4}$) considering k_e equal to 0.6 (Fig. 21(a)) and 1 (Fig. 21(b)). It can be seen from Fig. 21(b) that the proposed concrete correction factor of $k_e = 1$ for the flexural rigidity formula provides accurate predictions of the effective flexural rigidity of CFDSAT columns, as the points are closer to the diagonal line.

6. Conclusions

This study reported an experimental and numerical investigation on the flexural buckling behaviour of CFDSAT columns. A total of 8 columns were tested and 81 columns were numerically modelled, considering two combinations of outer and inner cross-section shapes, i.e., square-square and square-circular, different cross-section slenderness, member slenderness and concrete strengths. Based on the observed results, the following points can be summarised:

1) The predominant failure mode of all CFDSAT tested columns was flexural buckling. No inward or outward local buckling was identified at the outer tube of any specimen. Overall, the concrete infill effectively prevented the occurrence of inward local buckling.
2) The experimental axial load versus mid-height lateral displacement curves demonstrated good ductility of all CFDSAT specimens, which is attributed to the beneficial composite action of the three elements of the CFDSAT cross-sections.
3) It was shown that the developed FE model with a global imperfection amplitude of $L_e/1000$ accurately replicated the flexural buckling behaviour of CFDSAT columns. Hence, this model was adopted to conduct a numerical parametric study which included 81 specimens, to investigate the effect of hollow ratio, member slenderness, cross-section slenderness of hollow tubes and concrete compressive strength on the ultimate capacity of CFDSAT specimens.
4) The numerical parametric study results revealed that the cross-sectional dimensions of the outer tube, member slenderness and concrete compressive strength have significant influences on the ultimate load of CFDSAT columns. It was demonstrated that the larger cross-sectional dimensions of the outer tube and the higher concrete compressive strength substantially improved the ultimate capacity of the composite members. However, the variation of cross-sectional dimensions of the inner tube has a negligible effect on the ultimate load of the columns, as the inner tube provides the least flexural buckling resistance among the three components of the composite cross-sections.
5) In the absence of design standards for CFDSAT members, a design methodology was proposed with a design buckling curve to predict the ultimate load of CFDSAT columns according to the Eurocode 4 framework. It was demonstrated that the proposed design methodology with imperfection factor and limit of the horizontal plateau equal to 0.34 and 0.1, respectively is appropriate for the design of CFDSAT columns as it accurately predicts the ultimate load of the composite columns.
6) A revised concrete correction factor of $k_e = 1$ was suggested based on test and FE data for the formula of Eurocode 4 to determine the effective flexural rigidity of CFDSAT columns. It is concluded that by using the proposed value for k_e, the accuracy of the formula to predict the effective flexural rigidity of CFDSAT columns is improved by 35 %.

CRediT authorship contribution statement

Shafayat Bin Ali: Conceptualization, Methodology, Software, Validation, Formal analysis, Data curation, Investigation, Visualization, Writing – original draft. **George S. Kamaris:** Conceptualization, Supervision, Writing – review & editing, Funding acquisition, Project administration. **Michaela Gkantou:** Conceptualization, Supervision, Writing – review & editing, Funding acquisition.
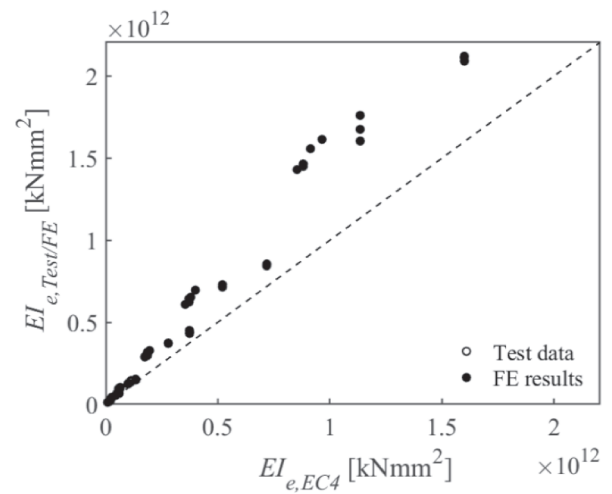
(a) Concrete correction factor $k_e = 0.6$
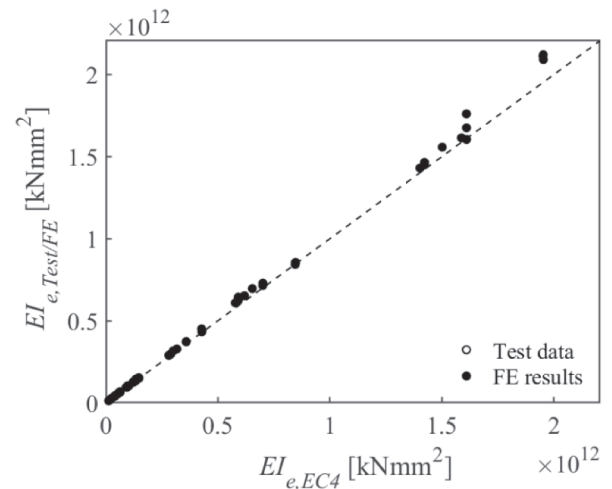
(b) Concrete correction factor $k_e = 1$

Fig. 21. Comparison of test and FE effective flexural rigidities ($EI_{e,Test/FE}$) of the specimens with the corresponding predicted values ($EI_{e,EC4}$) considering k_e equal to 0.6 and 1.

Declaration of Competing Interest

The authors declare that they have no known competing financial interests or personal relationships that could have appeared to influence the work reported in this paper.

Data availability

No data was used for the research described in the article.

Acknowledgements

References

[1] Wang F, Young B, Gardner L. Testing and numerical modelling of circular CFDST cross-sections with stainless steel outer tubes in bending. Eng Struct 2021;247: 113170.

[2] Alqawzai S, Chen K, Shen L, Ding M, Yang B, Elchalakani M. Behavior of octagonal concrete-filled double-skin steel tube stub columns under axial compression. J Constr Steel Res 2020;170:106115.

[3] Li W, Ren QX, Han LH, Zhao XL. Behaviour of tapered concrete-filled double skin steel tubular (CFDST) stub columns. Thin-Walled Struct 2012;57:37–48.

[4] Mazzolani FM. Aluminium alloy structures. 2nd ed. London Chapman Hall; 1995.

[5] Mazzolani FM. Competing issues for aluminium alloys in structural engineering. Prog Struct Eng Mater 2004;6(4):185–96.

[6] Georgantzia E, Gkantou M, Kamaris GS. Aluminium alloys as structural material: a review of research. Eng Struct 2021;227:111372.

[7] Georgantzia E, Ali SB, Gkantou M, Kamaris GS, Kansara KD, Atherton W. Flexural buckling performance of concrete-filled aluminium alloy tubular columns. Eng Struct 2021;242:112546.

[8] Ali SB, Kamaris GS, Gkantou M, Kansara KD, Hashim K. Numerical study of concrete-filled aluminium alloy tubular columns under eccentric compression. In IOP Conference Series: Materials Science and Engineering 2021;1058:012010.

[9] Ali SB, Kamaris GS, Gkantou M, Kansara KD. Concrete-filled and bare 6082–T6 aluminium alloy tubes under in-plane bending: experiments, finite element analysis and design recommendations. Thin-Walled Struct 2022;172:108907.

[10] Zhao XL, Grzebieta R. Strength and ductility of concrete-filled double skin (SHS inner and SHS outer) tubes. Thin-Walled Struct 2002;40:199–213.

[11] Tao Z, Han LH. Behaviour of concrete-filled double skin rectangular steel tubular beam–columns. J Constr Steel Res 2006;62:631–46.

[12] Tao Z, Han LH, Zhao XL. Behaviour of concrete-filled double skin (CHS inner and CHS outer) steel tubular stub columns and beam-columns. J Constr Steel Res 2004; 60:1129–58.

[13] Uenaka K, Kitoh H, Sonoda K. Concrete filled double skin circular stub columns under compression. Thin-Walled Struct 2010;48:19–24.

[14] Yan XF, Zhao YG. Compressive strength of axially loaded circular concrete-filled double-skin steel tubular short columns. J Constr Steel Res 2020;170:106114.

[15] Elchalakani M, Zhao XL, Grzebieta R. Tests on concrete filled double-skin (CHS outer and SHS inner) composite short columns under axial compression. Thin-Walled Struct 2002;40:415–41.

[16] Han LH, Tao Z, Huang H, Zhao XL. Concrete-filled double skin (SHS outer and CHS inner) steel tubular beam-columns. Thin-Walled Struct 2004;42(9):1329–55.

[17] Wang F, Young B, Gardner L. Experimental study of square and rectangular CFDST sections with stainless steel outer tubes under axial compression. J Struct Eng 2019;145(11):04019139.

[18] Wang F, Young B, Gardner L. Compressive testing and numerical modelling of concrete-filled double skin CHS with austenitic stainless steel outer tubes. Thin-Walled Struct 2019;141:345–59.

[19] Wang F, Young B, Gardner L. CFDST sections with square stainless steel outer tubes under axial compression: Experimental investigation, numerical modelling and design. Eng Struct 2020;207:110189.

[20] Han LH, Ren QX, Li W. Tests on stub stainless steel–concrete–carbon steel double skin tubular (DST) columns. J Constr Steel Res 2011;67(3):437–52.

[21] Wang F, Young B, Gardner L. Compressive behaviour and design of CFDST cross-sections with stainless steel outer tubes. J Constr Steel Res 2020;170:105942.

[22] Tziavos NI, Gkantou M, Theofanous M, Dirar S, Baniotopoulos C. Behaviour of grout-filled double-skin tubular steel stub-columns: numerical modelling and design considerations. Structures 2020;27:1623–36.

[23] Zhao XL, Tong LW, Wang XY. CFDST stub columns subjected to large deformation axial loading. Eng Struct 2010;32:692–703.

[24] Han LH, Li YJ, Lao FY. Concrete-filled double skin steel tubular (CFDST) columns subjected to long-term sustained loading. Thin-Walled Struct 2011;49:1534–43.

[25] Zheng Y, He C, Zheng L. Experimental and numerical investigation of circular double-tube concrete-filled stainless steel tubular columns under cyclic loading. Thin-Walled Struct 2018;132:151–66.

[26] Hassanein MF, Kharoob OF. Analysis of circular concrete-filled double skin tubular slender columns with external stainless steel tubes. Thin-Walled Struct 2014;79: 23–37.

[27] Sulthana UM, Jayachandran SA. Axial compression behaviour of long concrete filled double skinned steel tubular columns. Struct 2017;9:157–64.

[28] Zhao H, Wang R, Lam D, Hou CC, Zhang R. Behaviours of circular CFDST with stainless steel external tube: slender columns and beams. Thin-Walled Struct 2021; 158:107172.

[29] Ahmed M, Liang QQ, Hamoda A, Arashpour M. Behavior and design of thin-walled double-skin concrete-filled rectangular steel tubular short and slender columns with external stainless-steel tube incorporating local buckling effects. Thin-Walled Struct 2022;170:108552.

[30] Zhou F, Young B. Concrete-filled double-skin aluminum circular hollow section stub columns. Thin-Walled Struct 2018;133:141–52.

[31] Zhou F, Young B. Compressive strengths of concrete-filled double-skin (circular hollow section outer and square hollow section inner) aluminium tubular sections. Advances. Struct Eng 2019:1–17.

[32] Patel VI, Liang QQ, Hadi MNS. Numerical study of circular double-skin concrete-filled aluminum tubular stub columns. Eng Struct 2019;197:109418.

[33] Kissell J, Ferry R. Aluminum structures: a guide to their specifications and design. New York John Wiley Sons; 2002.

[34] BS EN 1994-1-1. Eurocode 4 (EC4): Design of composite steel and concrete structures. Part 1-1: General rules and rules for buildings. European Committee for Standardization (CEN), Brussels, 2004.

[35] BS EN 1999-1-1. Eurocode 9 (EC9): Design of aluminium structures. Part 1-1: General structural rules - General structural rules and rules for buildings. European Committee for Standardization (CEN), Brussels, 2007.

[36] BS En ISO. 6892–1. metallic materials – tensile testing – part 1: Method of test at room temperature. Brussels: European Committee for Standardization (CEN); 2009.

[37] Ramberg W, Osgood WR. Description of stress-strain curves by three parameters. Technical Note No. 902. Washington, D.C., USA: National Advisory Committee for Aeronautics, 1943.

[38] Hill HN. Determination of stress-strain relations from "offset" yield strength values. Technical Note No. 927; 1944.

[39] En BS. 12390–3. Testing hardened concrete. Compressive strength of test specimens. European Committee for Standardization (CEN), Brussels 2009.

[40] Karlsson Hibbitt, Sorensen, Inc. ABAQUS. ABAQUS/Standard User's Manual Volumes I-III and ABAQUS CAE Manual, 2016. Pawtucket (USA), Version 2016.

[41] Milan CC, Albareda-Valls A, Carreras JM. Evaluation of structural performance between active and passive preloading systems in circular concrete-filled steel tubes (CFST). Eng Struct 2019;194:207–19.

[42] Tao Z, Wang ZB, Yu Q. Finite element modelling of concrete-filled steel stub columns under axial compression. J Constr Steel Res 2013;89:121–31.

[43] Papanikolaou V, Kappos A. Confinement-sensitive plasticity constitutive model for concrete in triaxial compression. Int J of Solids Struct 2007;44(21):7021–48.

[44] Yu T, Teng J, Wong Y, Dong S. Finite element modeling of confined concrete-I: Drucker-Prager type plasticity model. Eng Struct 2010;32(3):665–79.

[45] Huang H, Han LH, Tao Z, Zhao XL. Analytical behaviour of concrete-filled double skin steel tubular (CFDST) stub columns. J Constr Steel Res 2010;66(4):542–55.

[46] Hordijk D. Local approach to fatigue of concrete (PhD Thesis). (Delft: Delft University of Technology); 1991.

[47] FIP. Ceb-Fip Model Code 1990. Ceb-Fip Model Code 1990. 1993.

[48] Bažant Z, Becq-Giraudon E. Statistical prediction of fracture parameters of concrete and implications for choice of testing standard. Cem Concr Res 2002;32:529–56.

[49] Mazzolani FM. Residual Stress Tests Alu-Alloy Austrian Profiles, ECCS Committee, Brussels, 1975 Technical Report, Doc 16-75-1.

[50] Zhou F, Young B. Numerical analysis and design of concrete-filled aluminum circular hollow section columns. Thin-Walled Struct 2012;50(1):45–55.

[51] Ali SB, Kamaris GS, Gkantou M. Flexural behaviour of concrete-filled double skin aluminium alloy tubes. Eng Struct 2022;272:114972.